



Nanosized iron and nickel oxide zirconia supported catalysts for benzylation of benzene: Role of metal oxide support interaction



Tarek T. Ali^{a,b}, Katabathini Narasimharao^{a,*}, Nesreen S. Ahmed^a, Sulaiman Basahel^a, Shaeel Al-Thabaiti^a, Mohamed Mokhtar^{a,c,**}

^a Department of Chemistry, Faculty of Science, King Abdulaziz University, P.O. Box 80203, Jeddah 21589, Saudi Arabia

^b Chemistry Department, Faculty of Science, Sohag University, P.O. Box 82524, Sohag, Egypt

^c Physical Chemistry Department, National Research Centre, El Buhouth St., Dokki, Cairo, Egypt

ARTICLE INFO

Article history:

Received 7 May 2014

Received in revised form 9 August 2014

Accepted 12 August 2014

Available online 20 August 2014

Keywords:

Zirconia

Benzylation

Metal oxide-support interaction

Acid sites

Dispersion

ABSTRACT

Nanocrystalline Fe_2O_3 and NiO mesoporous ZrO_2 supported catalysts were prepared and thermally treated at 500 °C. The efficacy of catalysts for catalyzing the benzylation of benzene using benzyl chloride was studied. The mesoporous ZrO_2 alone showed only benzyl chloride conversion of 44% after a reaction time of 600 min at 75 °C. An increase in the conversion of benzyl chloride to 49% was observed after loading 10 wt% of NiO on ZrO_2 . The conversion was further increased to 58% with the increase of NiO loading to 20 wt%. However, a drastic increase of conversion was observed after loading 10 wt% Fe_2O_3 on ZrO_2 , the conversion reached to 78% under identical reaction conditions. The increase of Fe_2O_3 loading to 20 wt% led to a significant increase in conversion of benzyl chloride to 91%. The characterization results showed that ZrO_2 support is mesoporous comprising monoclinic and tetragonal phases. The loading of the NiO or Fe_2O_3 led to phase transformation of ZrO_2 into cubic phase. Diffraction peaks due to Fe_2O_3 were not observed; in contrast, the presence of segregated NiO phase was observed in case of NiO supported ZrO_2 samples. The mesoporous ZrO_2 support maintained the stability of catalytically active Fe_2O_3 species after six reaction cycles. The enhanced catalytic activity of this catalyst is attributed to the presence of a greater degree of dispersion of Fe_2O_3 over ZrO_2 , higher redox potential and a greater degree of accessible surface Lewis acid sites.

© 2014 Elsevier B.V. All rights reserved.

1. Introduction

Diphenylmethane, also known as benzyl benzene, is a valuable intermediate in chemical industry due to its use in the dye and perfume manufacturing processes [1]. Friedel–Crafts benzylation of benzene using benzyl chloride to afford diphenylmethane is a well-known method to synthesize diphenylmethane. The commonly used homogeneous catalysts such as AlCl_3 , BF_3 , H_3PO_4 and H_2SO_4 suffer from several disadvantages including difficulty in separation, recovery, disposal of used catalyst, their corrosive nature and high toxicity. The development of reusable heterogeneous catalysts is necessary to overcome the problems associated with homogenous catalysts [2]. Clark et al. reported that Zn modified montmorillonite and nickel chlorides were highly active catalysts for Friedel–Crafts

alkylation [3]. Coq et al. indicated that highly acidic zeolite catalysts, such as HY and H-ZSM-5, show poor activity for the benzylation reaction, because of diffusion limitation caused by their microporous nature [4]. Choudhary et al. [5] has studied benzylation of benzene by benzyl chloride over Fe-, Zn-, Ga- and In-modified ZSM-5 type catalysts and the performance of the catalysts were attributed to their improved properties. The same authors also observed that Fe-containing mesoporous molecular sieves were active in benzylation of benzene and have better stability than the Fe-pillared clays [5].

Subsequently, research has been directed towards the preparation of mesoporous materials for the benzylation reaction [6]. Mesoporous catalysts exhibited better benzylation activity than microporous catalysts. However, the reported mesoporous materials possessed poor stability and weak acidity compared with zeolites. Therefore, development of mesoporous catalysts with high stability and strong acidity for benzylation reaction is a topic of interest [7].

Zirconium dioxide (ZrO_2) is an important material that has been used extensively for heterogeneous catalytic reactions and

* Corresponding author. Tel.: +966 500558045; fax: +966 26952292.

** Corresponding author. Tel.: +966 500558045; fax: +966 26952292.

E-mail addresses: katabathini@yahoo.com (K. Narasimharao),

mmokhtar2000@yahoo.com (M. Mokhtar).

in other applications because of its versatile structural and surface chemical properties as well as good thermal stability [8]. Furthermore, ZrO_2 has been reported to be a better catalyst and catalyst support than classical materials such as Al_2O_3 , SiO_2 and TiO_2 [9]. Very few studies have been devoted to use catalysts that contain iron oxide, nickel oxide and for benzylation of benzene. Koyande et al. performed benzylation of benzene and other aromatic compounds over sulfated ZrO_2 and Fe_2O_3 catalysts [10]. Shinde et al. [11] used different ferrites such as CuFe_2O_4 , NiFe_2O_4 , CoFe_2O_4 , ZnFeO_4 and MgFe_2O_4 for the benzylation of benzene.

Decades ago, Mizuno et al. [12] reported that highly dispersed ZrO_2 -supported Fe, Co, Cr and Cu oxides show very high catalytic activities for the reduction of NO by CO. It was evident that the superior performances of these catalysts are considered to be a consequence of specific metal oxide– ZrO_2 interactions [13]. The nature of interaction between metal/metal oxide and ZrO_2 has been much less extensively studied than the interaction involving other supports such as Al_2O_3 , SiO_2 and TiO_2 . Yamaguchi [14] have observed distinctly three different iron species on the surface of ZrO_2 support; two kinds of highly dispersed Fe^{3+} species and bulk Fe_2O_3 particles.

Dongare et al. [15] synthesized NiO-ZrO_2 by the sol-gel method and they used the catalysts for methane oxidation. The authors observed that increasing of NiO content to 20 mol% was accompanied by an increase of catalytic activity. They also indicated that solid solutions of Ni-Zr-O and highly dispersed NiO particles were present in the catalysts and responsible for high activity of these catalysts. The activity of the catalysts decreased when NiO content was further increased to 40 mol%. They suggested the decrease of activity was due to the formation of coarse NiO particles possessing the properties of bulk NiO .

It is well known that the high dispersion of catalytically active transition metal oxides and their uniform volume distribution is necessary to increase the interface between the phases. It was observed in the literature that a NiO-ZrO_2 sample with 20 wt% nickel oxide loading retained its cubic phase even after calcination at 1000 °C, indicating thermal stability of cubic NiO-ZrO_2 phase [15].

In a recent publication [16], we reported synthesis of nano-sized iron oxide supported on mesoporous ZrO_2 using a modified co-precipitation method. We observed that addition of 20 wt% of iron oxide to ZrO_2 led to formation of amorphous Fe_2O_3 on the surface of the ZrO_2 support and migration of Fe cations from the surface to the crystal lattice of ZrO_2 to stabilize the tetragonal phase. In continuation of our effort to develop stable solid acid catalysts for production of fine chemicals, it is our interest to synthesize, characterize nanosize supported mesoporous ZrO_2 materials and utilize them as catalysts for benzylation. In this paper, we synthesized nanocrystalline iron oxide and nickel oxide supported ZrO_2 catalysts and studied physico-chemical properties of catalysts to investigate the nature of interaction between metal oxide and ZrO_2 and its role in benzylation of benzene reaction.

2. Experimental

2.1. Materials

All reagents were analytical grade and used as received without purification. Zirconyl chloride octahydrate [($\text{ZrOCl}_2 \cdot 8\text{H}_2\text{O}$)], ferric nitrate nonahydrate [$\text{Fe}(\text{NO}_3)_3 \cdot 9\text{H}_2\text{O}$], nickel nitrate hexahydrate [$(\text{NiNO}_3)_2 \cdot 6\text{H}_2\text{O}$], aqueous ammonia solution and ethylenediamine [$\text{C}_2\text{H}_4 \cdot (\text{NH}_2)_2$] were purchased from Aldrich, U.K.

2.2. Synthesis of nanocrystalline mesoporous iron and nickel oxide-supported ZrO_2 materials

The nanocrystalline mesoporous ZrO_2 support was prepared by a modified sol-gel method using ethylenediamine (EDA) as gel protection agent. Iron and nickel support on nanocrystalline mesoporous ZrO_2 were prepared by conventional impregnation.

2.2.1. Method of preparation

In this method, EDA was used as gel protecting agent to prepare ZrO_2 support. Hundred milliliter of 0.88 molar EDA solution was added drop wise to the solution containing 26.1 g of $\text{ZrOCl}_2 \cdot 8\text{H}_2\text{O}$ in 100 mL of distilled water. The solution (pH of 10) was maintained at 50 °C in a water bath and subjected to ultrasonication for 5 h. Then the solution was kept for aging at 80 °C for 100 h to obtain a gel. The obtained gel was then washed with ethanol for four times and dried at 100 °C for 24 h.

Iron and nickel oxide supported ZrO_2 nanomaterials were prepared by impregnating the calculated amount of dried ZrO_2 powder with solutions of $\text{Fe}(\text{NO}_3)_3 \cdot 9\text{H}_2\text{O}$ or $\text{Ni}(\text{NO}_3)_2 \cdot 6\text{H}_2\text{O}$ that corresponded to 10.0 wt% and 20.0 wt% of iron or nickel oxide. The excess water was removed by slow drying and the dried materials were washed four times with distilled water. Portions of the synthesized materials were calcined at 500 °C with a ramp rate of 1 °C min⁻¹ and kept at this temperature for 3 h. The calcined materials were annotated using the following nomenclature: 10-FeZr, 20-FeZr, 10-NiZr and 20-NiZr for 10 wt% and 20 wt% iron and nickel oxides loaded ZrO_2 samples.

2.3. Characterization

The elemental composition of the catalysts was determined by ICP-AES, Optima 7300DV, Perkin Elmer Corporation, USA. The sample preparation for ICP-AES was as follows: about 100 mg of catalyst was placed in a PTFE beaker and then complete dissolution of the sample was achieved by adding 8 mL of 40% HF, 2 mL of HNO_3 and 2 mL of HCl and to this 15 mL of ultra-pure water was added and then PTFE beaker was placed in an ultrasonic bath for 10 min to obtain homogeneous dissolution. The solution was then rinsed into a centrifuge tube and centrifuged at 3000 rpm for 3 min. The clear supernatant was decanted and used to prepare 250 mL stock solution.

X-ray powder diffraction (XRD) studies were performed for all of the prepared solid samples using a Bruker diffractometer (Bruker D8 advance target). The patterns were obtained using copper $\text{K}\alpha_1$ and a monochromator ($\lambda = 1.5405 \text{ \AA}$) at 40 kV and 40 mA. The crystallite size of the zirconia phase was calculated using Scherrer equation (1):

$$D = B\lambda / \beta_{1/2} \cos \theta \quad (1)$$

where D is the average crystallite size of the phase under investigation, B the Scherrer constant (0.89), λ the wavelength of the X-ray beam used (1.5405 \AA), $\beta_{1/2}$ is the full width at half maximum (FWHM) of the diffraction peak and θ is the diffraction angle. The identification of different crystalline phases in the samples was performed by comparing the data with the Joint Committee for Powder Diffraction Standards (JCPDS) files. The Raman spectra of samples were measured with a Bruker Equinox 55 FT-IR spectrometer equipped with an FRA106/S FT Raman module and a liquid N_2 cooled Ge detector using the 1064 nm line of an Nd:YAG laser with an output laser power of 200 mW. SEM measurements were carried out using a JEOL JSM840A system. For SEM, each of the powders was attached to an aluminum block using double sided carbon tape. The samples were then coated in gold to make them conductive and compatible with the SEM technique.

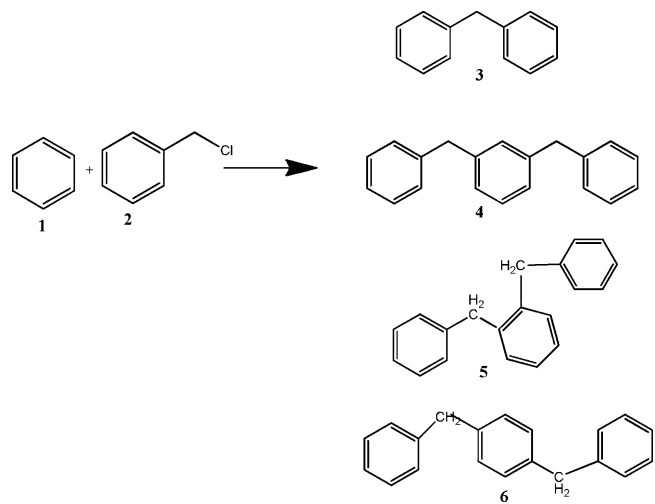
A Philips CM200FEG microscope, 200 kV, equipped with a field emission gun was used for TEM and HRTEM analyses. The coefficient of spherical aberration was $C_s = 1.35$ mm. The information limit was better than 0.18 nm. High-resolution images with a pixel size of 0.044 nm were taken with a CCD camera. The textural properties of the prepared samples were determined from nitrogen adsorption/desorption isotherm measurements at -196°C using a model NOVA 3200e automated gas sorption system (Quanta-chrome, U.S.A.). Prior to measurement, each sample was degassed for 6 h at 150°C . The specific surface area, S_{BET} , was calculated by applying the Brunauer–Emmett–Teller (BET) equation. The average pore radius was estimated from the relation $2V_p/S_{\text{BET}}$, where V_p is the total pore volume (at $P/P^0 = 0.975$). Pore size distribution over the mesopore range was generated by the Barrett–Joyner–Halenda (BJH) analysis of the desorption branches, and the values for the average pore size were calculated. The XPS measurements were carried out using a SPECS GmbH X-ray photoelectron spectrometer. Prior to analysis, the samples were degassed under vacuum inside the load lock for 16 h. The binding energy of the adventitious carbon (C 1s) line at 284.6 eV was used for calibration, and the positions of other peaks were corrected according to the position of the C 1s signal. For the measurements of high resolution spectra, the analyzer was set to the large area lens mode with energy steps of 25 meV and in Fixed Analyzer Transmission (FAT) mode with pass energies of 34 eV and dwell times of 100 ms. The photoelectron spectra of the samples were recorded with the acceptance area and angle of 5 mm in diameter and up to $\pm 5^\circ$, respectively. The base pressure during all measurements was 5×10^{-9} mbar. A standard dual anode excitation source with Mg K α (1253.6 eV) radiation was used at 13 kV and 100 W.

DRIFT spectra of calcined catalysts obtained at room temperature using Perkin-Elmer Spectrum 100 FTIR spectrometer. Then, the samples were subjected to pyridine adsorption analysis. The analysis was carried out over a catalyst disk which was treated under vacuum for 5 h. Later, the sample was treated with pyridine vapor and finally heated at 100°C under vacuum for 30 min. DRIFT spectra were collected at room temperature. The density of Lewis acid sites for each catalyst was calculated via integration of the area of the absorption band showing the maximum values of intensity at 1446 cm^{-1} . Integrated absorbance of the band was obtained using the appropriate software by applying the corresponding extinction coefficient and normalized by the weight of the samples.

Temperature programmed reduction experiments were performed using a Micromeritics AutoChem 2910 instrument. A calculated amount of catalyst was initially treated with 10% O_2 –90% Ar at 300°C for 30 min, and then the sample tube was purged with Ar gas. The sample temperature was brought down to room temperature (25°C) by passing air into the furnace. Then, the flow of the gas was changed to 5% H_2 + 95% Ar and the sample temperature increased to 600°C at the rate of $5^\circ\text{C}/\text{min}$. TPR patterns were obtained by recording the TCD signal with respect to the time and temperature.

2.4. Benzylation of benzene using benzyl chloride

The liquid phase benzylation of benzene with benzyl chloride (BC) was carried out in a three necked round-bottomed flask equipped with a reflux condenser and electrically heated in a precisely controlled oil bath under atmospheric pressure. In a typical run, 13 mL of benzene was added to 50 mg catalyst (which had been activated overnight at 100°C). The reaction mixture was maintained for 30 min at the required reaction temperature, and then 1 mL of benzyl chloride was added. The moment was regarded as initial reaction time. Liquid samples were withdrawn at regular intervals and analyzed by gas chromatography (HP-6890) equipped with a FID detector and HP-5 capillary column. The products were



Scheme 1. Reaction pathway of benzylation of benzene with benzyl chloride.

also identified by GC-MS (HP-5975-C) analysis. Since benzene was in excess, conversion was calculated based on the benzylating reagent, i.e., BC. The selectivity to the product diphenylmethane (DPM) was expressed as the amount of particular product divided by amount of total products and multiplied by 100.

3. Results and discussion

3.1. Benzylation activity

Benzylation of benzene (1) with benzyl chloride (2) as an alkylating agent produces mainly diphenylmethane (3) (Scheme 1). As the Friedel–Crafts reaction is always accompanied by di- and poly-alkylations, due to higher reactivity of the product than the reactant, the benzylation reaction could also give dibenzylation products (4, 5, 6) as side products. Thus, dibenzylbenzene, tribenzylbenzene, etc., may be formed in the reaction, dibenzylbenzene being the most prominent side products.

The conversion of benzyl chloride with reaction time over ZrO_2 , iron oxide and nickel oxide supported ZrO_2 catalysts at 75°C is shown in Fig. 1. As expected, ZrO_2 support offered low catalytic activity, with a benzyl chloride conversion of 43.8% after a reaction time of 600 min. A slight increase of conversion of benzyl chloride

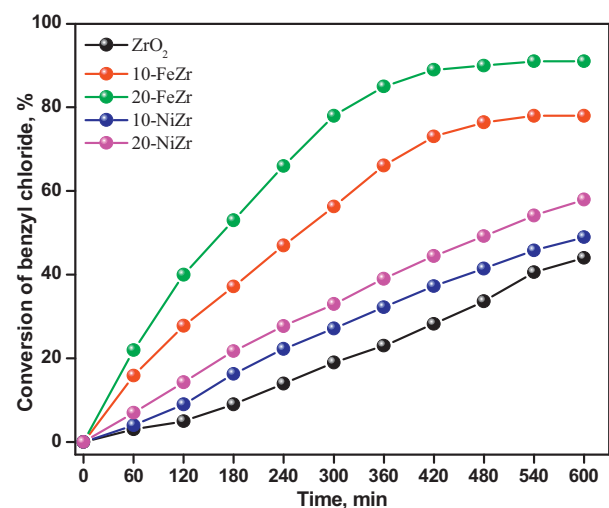


Fig. 1. The conversion of benzyl chloride with the reaction time over ZrO_2 , iron oxide and nickel oxide supported ZrO_2 catalysts, reaction temperature; 75°C .

Table 1

Conversion of benzyl chloride and reaction rate per unit surface area of ZrO_2 and iron oxide and nickel oxide supported ZrO_2 catalysts at different reaction temperatures for 600 min of reaction time.

Catalyst	65 °C		70 °C		75 °C	
	Conversion (%)	\bar{k} ($\text{min}^{-1} \text{m}^{-2} \text{g}$), 10^{-5}	Conversion (%)	\bar{k} ($\text{min}^{-1} \text{m}^{-2} \text{g}$), 10^{-5}	Conversion (%)	\bar{k} ($\text{min}^{-1} \text{m}^{-2} \text{g}$), 10^{-5}
ZrO_2	29(95) ^a	0.67	37(95)	0.93	43.8 (95)	1.30
10-FeZr	45(98)	1.53	66(98)	2.64	78(98)	3.44
20-FeZr	54(99)	2.18	80(99)	3.88	91(99)	5.55
10-NiZr	37(96)	0.72	42(96)	0.95	49(97)	1.21
20-NiZr	42(97)	0.49	53(97)	0.79	58(98)	0.98

^a The values in the parenthesis represents selectivity to diphenylmethane.

Table 2

Activation energies (E_a , E_a^*) and frequency factor (A) for the catalytic reaction conducted over different catalysts.

Catalyst	E_a (kJ mol^{-1})	$\ln A$	E_a^* (kJ mol^{-1})	TON	TOF (h^{-1})
ZrO_2	64.74	15.25	64.74	941.8	94.2
10-FeZr	79.27	21.67	60.98	13,628.5	1362.9
20-FeZr	91.35	26.39	59.58	9034.1	903.4
10-NiZr	50.53	16.51	63.53	7871.9	787.2
20-NiZr	66.66	10.69	63.07	5768.9	576.9

Reaction conditions, temperature = 75 °C, benzene/benzyl chloride stoichiometric ratio = 15 and 0.1 g of catalyst.

E_a = Apparent activation energy.

E_a^* = Real activation energy.

(44%) was observed upon loading of 10 wt% nickel oxide on ZrO_2 . The conversion was further increased to 58% with the increase of nickel oxide loading to 20 wt%. Conversely, a significant increase of activity was observed after loading 10 wt% iron oxide on ZrO_2 support, the benzyl chloride conversion reached 78% after a reaction time of 600 min. Increase of iron oxide loading to 20 wt% led to a significant increase in conversion of benzyl chloride to 91%.

The conversion of benzyl chloride and rate of reaction per unit surface area of ZrO_2 and iron and nickel oxides supported ZrO_2 catalysts at different reaction temperatures are presented in Table 1. It is clear that when the bulk ZrO_2 support was used as a catalyst, only 43.8% conversion was observed after 600 min at 75 °C clearly indicating that the presence of active metal oxide species is essential to obtain high conversion in this reaction.

The benzyl chloride conversion increased with increasing temperature for all the catalysts. In terms of the rates of benzyl chloride conversion per unit surface area of catalysts (Table 1), 20-FeZr catalyst showed the highest benzylation rate, followed by 10-FeZr and then 10-NiZr and ZrO_2 . It is interesting to note that 20-NiZr catalyst offered less benzyl chloride conversion rate than bulk ZrO_2 support. These rates per unit surface area were consistent among all catalysts; however, the greatest difference was observed at high reaction temperature (75 °C) where the 20-FeZr catalyst was more active than any other catalysts. A noticeably high difference in activity can be observed in iron and nickel oxide ZrO_2 supported catalysts with two different compositions; thus, it can be assumed that the catalytic activity of these catalysts in benzylation of benzene was affected by their content and physico-chemical properties. The kinetic data for the benzylation of benzene reaction in excess of benzene [stoichiometric ratio (benzene/benzyl chloride) = 15] over all the catalysts could be fitted well to a pseudo-first-order rate law: $\ln[1/(1-x)] = k_a(t - t_0)$, where k_a is the apparent first-order rate constant, x is the fractional conversion of benzyl chloride, t is the reaction time and t_0 is the induction period corresponding to the time required for reaching equilibrium temperature. A plot of $\ln[1/(1-x)]$ as a function of time was presented in Fig. 2 (A). It is shown from this figure and the data presented in Table 2 that the reaction rate constant k_a for 20-FeZr catalyst is five times higher than that of pure ZrO_2 and twice that for 20-NiZr. Additionally, the turnover frequency (TOF) was estimated based on the mole number of benzyl chloride converted per mole metals per second. The value of TOF was 94 h^{-1} for ZrO_2 ,

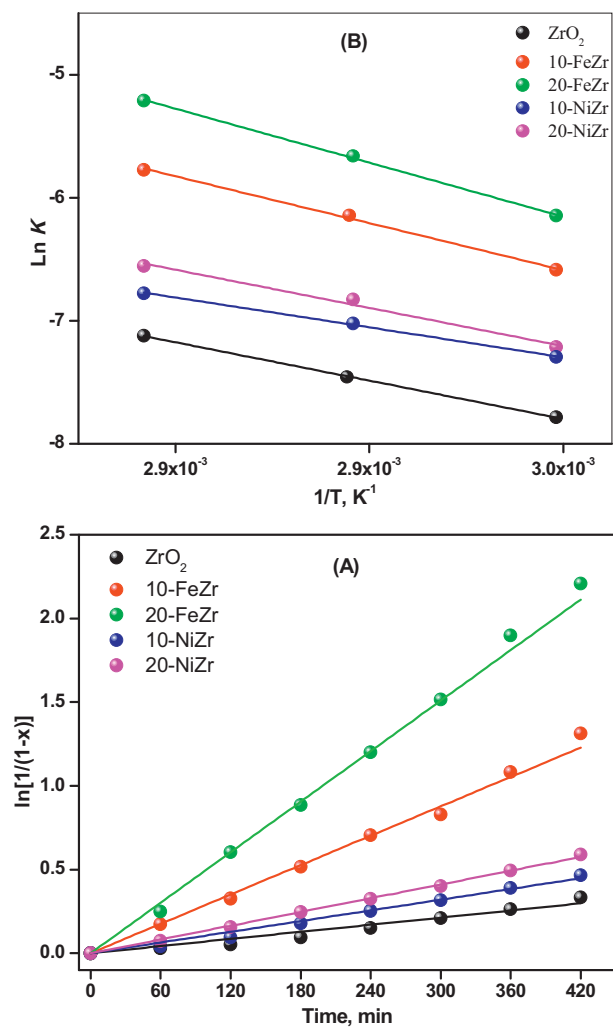


Fig. 2. (A) Plot of $\ln[1/(1-x)]$ as a function of the reaction time. (B) Arrhenius plots of benzyl chloride conversion reaction for all the catalysts.

903 h⁻¹ for 10FeZr, 1362 h⁻¹ for 20-FeZr, 787 h⁻¹ for 10NiZr and 576 h⁻¹ for 20-NiZr, respectively (Table 2). Based on the comparison of TOF data, it can be seen that the enhancement of catalytic performance is much greater for iron oxide supported ZrO₂ catalysts. For instance, the TOF of 20-FeZr is 15 times higher than that of ZrO₂, 2.3 times that of 20-NiZr. The dependency of TOF on the iron oxide loading apparently suggests the formation of several Fe interaction species having different intrinsic activities for the reaction. The selectivity to DPM is similar for all the catalysts. The obtained products comprised mainly DPM (above 95%), with a small amount of DBE (below 4%). Polyaromatic condensation compounds, 5 and 6 were not detected in the product analysis. Friedel–Crafts alkylation is an aromatic electrophilic substitution reaction in which the carbocation is formed by the complexation of alkyl halide with the catalyst. The carbocation attacks the aromatic species for alkylation and, hence, formation of the carbocation is an important step in the reaction mechanism. In general, Lewis acidic centers on the catalyst surface facilitate the carbocation formation. The studied NiZr and FeZr catalysts possessed mainly Lewis acid centers (as shown later), which are responsible for selective alkylation reaction.

The activity has significantly increased with increase in Fe loading from 10 wt% to 20 wt%. It would be interesting to see how it will show when the Fe loading is further increased. To obtain a better insight, we prepared 30 wt% iron oxide ZrO₂ (30-FeZr) sample and tested for benzylation of benzene reaction; however, 30-FeZr sample offered less conversion than 20-FeZr catalyst. Thirty-FeZr sample showed 68.2% conversion of benzyl chloride at 75 °C. The decrease of activity might be due to the fact that the 30-FeZr is behaving like a bulk iron oxide. It is well known that when the loading of active component exceeds beyond support monolayer coverage, the supported catalyst attains nature of bulk oxide.

It was previously mentioned that benzene was taken in excess in the reaction mixture and the benzyl chloride was a limiting reactant. The concentration of the benzyl chloride may not be uniform within the catalyst particles due to intra-particle diffusional resistance. For this reason, the effect of intra-particle resistance or pore diffusional resistance was determined for all the catalysts. Doraiswamy and Sharma [17] developed differential equations to determine the intra-particle resistance. The values of the Theile modulus (ϕ) and effectiveness factor (η) for ZrO₂, iron oxide and nickel oxide supported ZrO₂ catalysts were calculated according to the following equations:

$$\phi = (kR^2/D_e)^{1/2} \quad (2)$$

where D_e is the diffusivity, k the rate constant, R the radius of particle; the particle size of all the investigated catalysts was calculated from TEM measurements:

$$\eta = (1/5 [\cot 3\phi + 1/3\phi]) \quad (3)$$

The effective diffusivity (D_e) of benzyl chloride into benzene can be calculated using the Wilkinson–Chan equation

$$D_e = 7.4 \times 10^{-8} [(XM)^{0.5} / V_b^{0.6}] [T/\mu] \quad (4)$$

where X is the association constant of benzene, M the molecular weight of benzene, T the temperature, V_b the molar volume of benzyl chloride and μ the viscosity of benzene.

It was observed that the Theile modulus and the effectiveness factor are around 1 for all the investigated catalysts, which means that there was no intra-particle diffusional resistance in case of all these catalysts.

The determination of the activation energy (E_a) for benzylation of benzene over iron and nickel oxide supported ZrO₂ catalysts can provide an insight on the role of metal (Fe or Ni) oxide in the benzylation reaction. The reaction rate constant (k_a) for benzylation

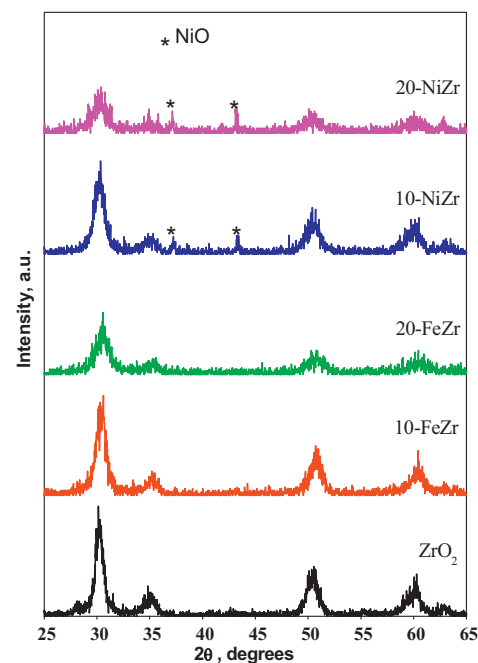


Fig. 3. Powder X-ray diffraction patterns of all the catalysts.

reaction at different temperatures (65 °C, 70 °C and 75 °C) for all the catalysts was determined by using the Arrhenius equation.

Fig. 2 (B) shows the Arrhenius plots of benzylation reaction for all the catalysts. The observed E_a values are tabulated in Table 2. The apparent activation energy for the 20-FeZr and 10-FeZr catalysts, which showed the highest catalytic activity, is 91.3 kJ mol⁻¹ and 79.2 kJ mol⁻¹, respectively. In contrast, the calculated apparent activation energy for pure ZrO₂ that showed less activity is 64.7 kJ mol⁻¹. These results did not represent the superior catalytic activity of 20-FeZr and 10-FeZr catalysts. This discrepancy has been solved by re-computing E_a values taking into consideration the possible changes in the values of the pre-exponential factor (A) in the Arrhenius equation [18]. Column 3 of Table 2 includes the ln A values of for all the catalysts after re-computation. It is observed that the increase in the ' E_a ' values for iron oxide supported catalysts results mainly, from the increase in the value of ' A '. The real activation energy (E_a^*) is the same as apparent activation energy for pure ZrO₂ sample; however, E_a^* values for 20-FeZr and 10-FeZr catalysts higher than 10-NiZr, 20-NiZr and ZrO₂ samples.

The difference in catalytic activity between the iron and nickel oxide ZrO₂ supported catalysts possibly due to the difference in nature of interaction between these oxides with ZrO₂ support. A detailed characterization of catalysts is required to make the reason clear. Importantly, iron oxide ZrO₂ supported catalysts exhibited remarkably enhanced catalytic activity, which almost ended this reaction after a reaction time of 650 min.

3.2. Powder X-ray diffraction (XRD) analysis

The wide angle XRD patterns of ZrO₂, 10-FeZr, 20-FeZr, 10-NiZr and 20-NiZr samples calcined at 500 °C are shown in Fig. 3. The (101)_t and (111)_m reflections centered at 30.2° and 28.2° 2θ positions clearly indicate the coexistence of tetragonal and monoclinic phases in the pure ZrO₂ sample. All of the reflections of the XRD patterns of 10-FeZr and 20-FeZr samples can be indexed to the standard pattern of the pure cubic phase of ZrO₂. Diffraction peaks at 2θ = 30.3°, 35.14°, 50.48° and 60.2° reveal the presence of (111), (200), (220) and (311) planes, respectively, of cubic ZrO₂ according to JCPDS CAS number 27-0997. No diffraction

peaks corresponding to the iron oxides were observed in the XRD patterns, suggesting that the iron oxide might be well dispersed on ZrO_2 or incorporated into the ZrO_2 crystal lattice.

Nickel oxide supported catalysts (10-NiZr and 20-NiZr) exhibited similar diffraction peaks due to cubic ZrO_2 structure as iron oxide supported samples. These results indicate that addition of iron oxide and nickel oxide suppressed the formation of monoclinic phase. Sharp diffraction peaks due to cubic NiO were also observed in both 10-NiZr and 20-NiZr samples. It is interesting to note that the intensity of diffraction peaks due to cubic NiO was increased with increase of nickel oxide loading from 10 wt% to 20 wt%. This observation is an indication that NiO was agglomerated on the ZrO_2 surface.

The average crystallite size of pure ZrO_2 , 10-FeZr, 20-FeZr, 10-NiZr and 20-NiZr samples were calculated using Scherrer's equation. The calculated average crystalline size of all the samples according to X-ray line broadening analysis was 21 nm for ZrO_2 . The size of ZrO_2 after loading 10 wt% iron oxide was 21.5 nm and it was increased to 35 nm after 20 wt% loading. Apparently, there was no obvious change with 10 wt%, while the size of ZrO_2 particles became large by doubling the iron oxide loading. A similar phenomenon was observed for nickel oxide supported ZrO_2 samples crystals, the size of 10-NiZr was 30 nm and 42 nm for 20-NiZr. Obviously, nickel oxide supported catalysts possessed the largest crystallite size.

The assignment of cubic and tetragonal structures, based solely on the X-ray diffraction analysis, can be misleading because ' a_0' of the cubic and tetragonal structures are very similar ($a_0 = 0.5124 \text{ nm}$ for cubic, and $a_0 = 0.5094 \text{ nm}$ for tetragonal structures) [19]

3.3. Raman spectroscopy

Raman spectroscopy is a very useful tool to differentiate the ZrO_2 phases presented in the sample. It has been reported that tetragonal ZrO_2 exhibits typical Raman bands at 148, 263, 325, 472, 608 and 640 cm^{-1} , with a strong band at 263 cm^{-1} [20]. Monoclinic ZrO_2 exhibits bands at 140, 173, 185, 216, 260, 301, 328, 342, 471, 500, 553 and 632 cm^{-1} , with strong bands at 173, 185 and 472 cm^{-1} [21].

Gazzoli et al. [22] reported that the Raman peak at 151 cm^{-1} is common for both of tetragonal and cubic phases and cubic ZrO_2 presents a strong band between 607 and 617 cm^{-1} . Fig. 4 shows the Raman spectra of all the samples. The pure ZrO_2 sample showed stronger peaks at 262 cm^{-1} and 637 cm^{-1} along with other peaks which can be assigned to characteristic tetragonal ZrO_2 phase and also low intensity major peaks corresponding to monoclinic ZrO_2 . The peaks corresponding to tetragonal and monoclinic phases disappeared for iron oxide and nickel oxide supported ZrO_2 samples, which indicates the absence of tetragonal ZrO_2 in these samples. The presence of the Raman peaks centered at 151 , 242 and 607 cm^{-1} can be observed in iron oxide and nickel oxide supported ZrO_2 samples, these peaks are attributed to the characteristic bands of cubic ZrO_2 [23]. Therefore, the pure ZrO_2 sample is a mixture of tetragonal and monoclinic ZrO_2 ; in contrast, iron oxide and nickel oxide supported ZrO_2 samples are mainly cubic.

3.4. TEM analysis

The TEM micrographs of pure ZrO_2 , 10-FeZr, 20-FeZr, 10-NiZr and 20-NiZr, samples are presented in Fig. 5. The analyses revealed that ZrO_2 , 10-NiZr and 20-NiZr samples possessed agglomerated nanocrystalline particles with close packing arrangement; however, 10-FeZr and 20-FeZr showed individual particles with well resolved and irregular spherical and worm like

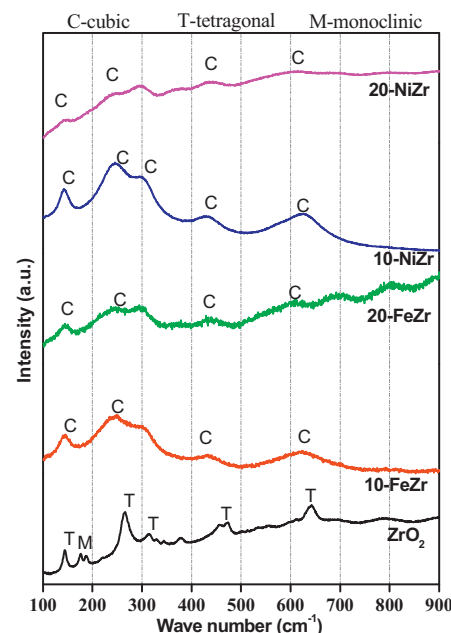


Fig. 4. Raman spectra of all the catalysts.

morphology. The images of 10-FeZr and 20-FeZr samples also showed the mesoscopic void spaces generated due to the packing of the ZrO_2 particles which lead to the porosity in the material. The particles in these samples are found to have a size between 20 nm and 30 nm. This estimation is in agreement with measurement for crystallite sizes obtained by X-ray diffraction line broadening through Scherer's equation. It also appears that the average size of the primary particles was increased with loading iron oxide or nickel oxide. The image also shows wormhole-like pore channel for the typical mesoporous ZrO_2 sample. The cubic phase ZrO_2 nanoparticles in 10-FeZr and 20-FeZr samples is uniformly distributed showing less agglomeration than the 10-NiZr and 20-NiZr samples. The TEM image of 20-FeZr sample reveals that the average particle size of the cubic phase ZrO_2 is about 20–25 nm.

The Raman spectroscopy results reveal that loading of 10 wt% nickel oxide is able to stabilize cubic phase to a greater extent at 500°C . The increased concentration of the nickel oxide helps nucleation of crystallites and enhances particle growth (XRD analysis). The particle size is found to be larger in 20-NiZr sample compared to the 10-NiZr sample.

3.5. HRTEM analysis

Cubic ZrO_2 lattices with interplanar spacing of 0.296 nm corresponding to the (1 1 1) spacing of the cubic phase [24] are observed in the HRTEM images of 20 wt% iron oxide and nickel oxide supported ZrO_2 samples (inset of TEM images of 20-FeZr and 20-NiZr, Fig. 5).

Formation of the structural defects was also observed in the HRTEM micrographs of iron supported ZrO_2 samples. Many lattice defects appeared in the boundaries of the crystals as shown in HRTEM images. Creation of the lattice defects in the structure is suggested to be mainly associated with the incorporation of the ethylenediamine in the solid during the synthesis by strong interactions between the hydroxyl groups and ethylenediamine head groups [25]. After calcination at 500°C , the incorporated EDA species were decomposed, generating some lattice defects in the corresponding locations.

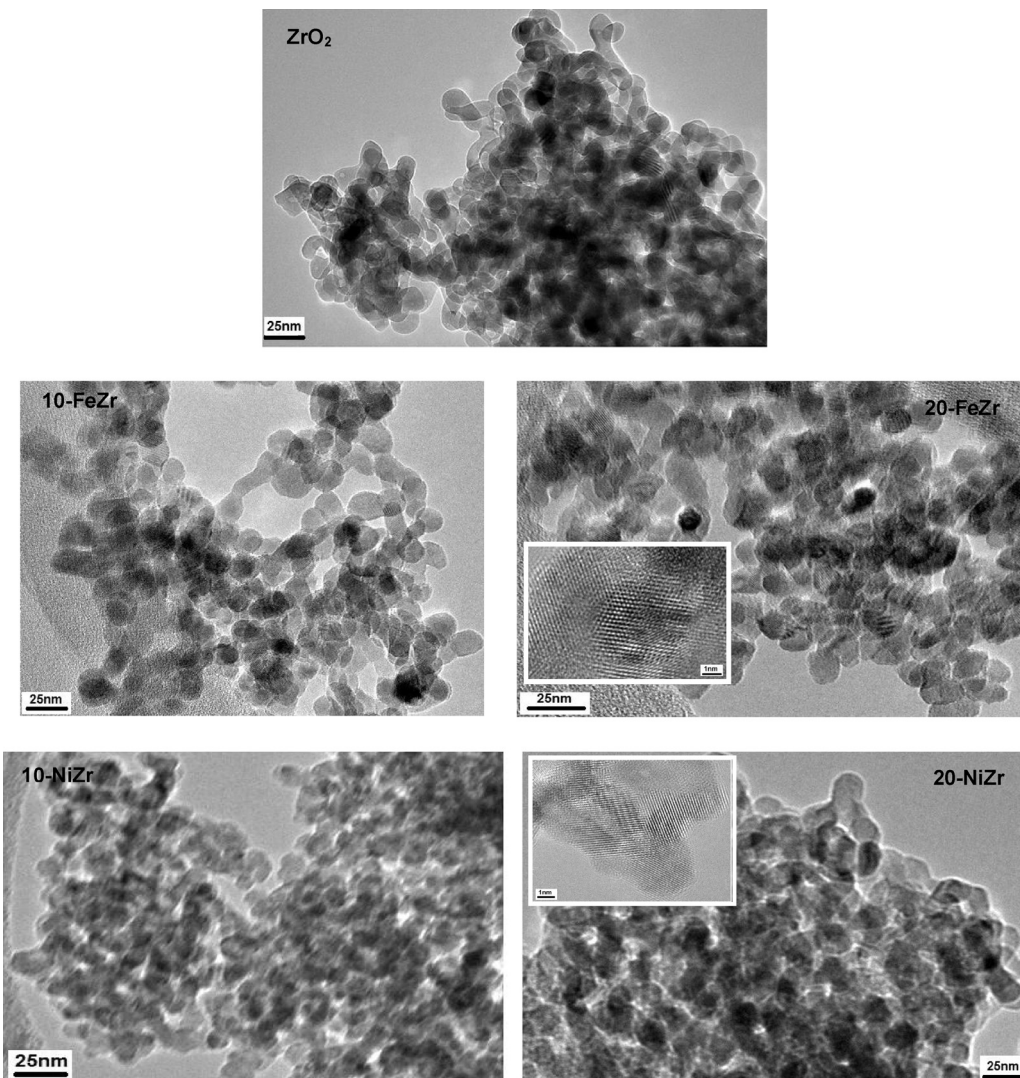


Fig. 5. TEM images of all the catalysts. Inset HRTEM images of 20-FeZr and 20-NiZr catalysts.

3.6. Nitrogen physisorption

Nitrogen adsorption–desorption isotherms of pure ZrO_2 , 10-FeZr, 20-FeZr, 10-NiZr and 20-NiZr samples are presented in supplementary information (Fig. S1). The type IV isotherms with H1 hysteresis loops for these samples were observed, indicating the existence of the mesopore structure in these samples. The appearance of a well-defined hysteresis loop associated with irreversible capillary condensation in the mesopores of the P/P^0 region from 0.4 to 1.0 suggests the presence of textural mesoporosity arising from non-crystalline intra-aggregate voids and spaces formed by interparticle contacts between the particles.

Brunauer–Emmett–Teller (BET) surface area, average pore diameter, and pore volume of the materials estimated from physisorption experiments are tabulated in Table 3. The order of surface areas of catalysts was as follows: 20-NiZr ($143 \text{ m}^2 \text{ g}^{-1}$) > 20-FeZr ($98 \text{ m}^2 \text{ g}^{-1}$) > 10-NiZr ($94 \text{ m}^2 \text{ g}^{-1}$) > 10-FeZr ($90 \text{ m}^2 \text{ g}^{-1}$) > ZrO_2 ($60 \text{ m}^2 \text{ g}^{-1}$). It is usually agreed that support with large surface area is favorable to disperse the active component on its surface. In general, loading of metal oxide is responsible for lowering of specific surface area of the support due to surface coverage and pore blocking by the impregnated phase [26]; interestingly, an increase of the specific surface area was observed after supporting the iron and nickel oxides on ZrO_2 . This is probably due to the fact that we used

a bi-functional ethylene diamine which acted as precipitating agent to precipitate ZrOCl_2 into ZrO(OH)_2 and colloidal protecting agent for ZrO(OH)_2 gel [27]. Impregnation of iron and nickel precursors to the ethylene diamine protected ZrO(OH)_2 gel and subsequent calcination yielded porous material which contained support and metal nanoclusters.

Relatively, nickel supported ZrO_2 catalysts possessed higher surface areas than iron supported ZrO_2 catalysts. It is known that the particle size of the dispersed metal oxide play an important role in textural properties of the total catalyst [5]. It is our argument that after ZrO_2 was impregnated with iron nitrate solution, Fe^{3+} could have been interacted with abundant hydroxyl groups on the surface of ZrO_2 , which promoted the uniform iron dispersion on it and reduce the size of iron oxide particles [28]. However, when ZrO_2 was impregnated with nickel nitrate solution, the interaction of nickel with the surface of ZrO_2 might not be as strong as iron [29]. This would promote the aggregation of Ni and lead to formation of large Ni particles during the calcination and subsequently led to an increase of interparticle voids (as observed in TEM analysis).

Deshmane and Adewuyi [30] synthesized nanocrystalline mesoporous ZrO_2 and sulfated ZrO_2 with high surface area and remarkable thermal stability using ethylene diamine and zirconyl chloride octahydrate. The authors discussed the inter-relationship between the preparation conditions and their crystalline and

Table 3

Textural properties of catalysts from N₂ physisorption and chemical composition of catalysts from ICP-AES and XPS analysis.

Catalyst	S _{BET} (m ² g ⁻¹)	V _p (cm ³ g ⁻¹)	Av. pore diameter (Å)	ICP-AES chemical analysis (Mass%)			XPS chemical analysis (Mass%)		
				Zr	Fe	Ni	Zr	Fe	Ni
ZrO ₂	62	0.1679	3.7	68.4	–	–	67.8	–	–
10-FeZr	90	0.1935	5.9	60.3	8.3	–	59.4	5.6	–
20-FeZr	98	0.2107	4.8	54.7	17.2	–	52.6	12.5	–
10-NiZr	94	0.1485	3.7	58.0	–	9.0	57.5	–	7.0
20-NiZr	143	0.1751	3.7	50.0	–	19.2	48.0	–	15.5

porous nature of ZrO₂. They observed that upon heat treatment, initially formed tetragonal ZrO₂ transforms into the monoclinic phase with reduction or breakage of the crystalline particles. The decrease in the surface area with increase in treatment temperature is due to the collapse of the mesopores induced by inter-crystalline sintering.

The pore-size distribution plots calculated using the BJH (Barrett–Joyner–Halenda) equation from the adsorption branch of the isotherms of all the samples are presented in supplementary information (Fig. S2). The pore-size distribution (PSD) measurements show that ZrO₂ sample has a narrow peak centered on 3.5 nm and broader PSD peak in the range of 4–16 nm pore diameter. The pore size distribution of the iron oxide supported ZrO₂ samples shows bi-modal pore distribution; in contrast, the nickel oxide supported ZrO₂ samples exhibits a well-defined microstructure with a relatively narrow pore-size distribution in the range of 3–3.5 nm without any mesopores.

Based on these data, ZrO₂ and iron oxide supported ZrO₂ samples can be described as mesoporous materials with broad pore size distribution. In contrast, the nickel oxide supported ZrO₂ has a well-developed microporous textural structure with a narrow pore size distribution.

3.7. X-ray photoelectron spectroscopy (XPS)

XPS was used to obtain further information about the valence/oxidation state of the elements and the surface composition of all the catalysts. Fig. 6(A) shows the O (1s) photoelectron transition diagram for all the samples. All the samples including pure ZrO₂ showed a single O (1s) peak. However, the binding energy of this peak for pure ZrO₂ sample is 530.2 eV and it was shifted to 530 eV for the iron oxide and nickel oxide supported ZrO₂ samples. Navio et al. [31] assigned a binding energy of 530.0 eV to the Zr–O–Zr bonding for iron oxide supported ZrO₂ catalysts. The lower value for O (1s) for the supported samples may be due to the presence of iron oxide or nickel oxide phases on the external surface of the ZrO₂ support. Wagner et al. [32] also observed a lower binding energy value of 0.8 eV for O (1s) from Fe₂O₃ in comparison with O (1s) from ZrO₂.

The Zr (3d_{5/2}) components for all the samples are shown in Fig. 6(B). The pure ZrO₂ sample showed a peak at 182.3 eV, which was shifted to 181.9 eV for the iron oxide and nickel oxide supported ZrO₂ samples. The change in coordination number of Zr atoms (tetragonal to cubic) is confirmed by the change in the measured binding energies (BE) of Zr 3d_{5/2} core levels. The BE for Zr in ZrO₂ sample is very close to the theoretical value for the Zr in ZrO₂ reported in the literature [33]. This value was decreased for 10-FeZr, 20-FeZr, 10-NiZr and 20-NiZr samples. The decrease of BE value can be interpreted in terms of electron transfer from Fe²⁺ or Ni²⁺ to Zr⁴⁺ [34]. This observation is in consistent with the XRD and Raman analyses, where it was shown that impregnation of iron oxide and nickel oxide caused the structural transformation of ZrO₂.

The deconvoluted spectra of Fe (2p_{3/2}) components for 10-FeZr and 20-FeZr samples are shown in Fig. 6(C). Wandelt et al. [35] also reported that the XPS Fe 2p_{3/2} characteristic binding energies for Fe⁰, Fe²⁺ and Fe³⁺ species generally appear at 707, 710 and 711 eV, respectively. It was also reported that Fe³⁺ 2p_{3/2} binding energy for bulk Fe₂O₃ is 711 eV, while Fe²⁺ 2p_{3/2} binding energy for bulk Fe₂O₃ is 709.7 eV [35]. Brundle et al. [36] observed a satellite peak for Fe³⁺ and Fe²⁺ at 719.8 and 715.0 eV, respectively. The binding energy of Fe metal appears generally around 706.4 eV [37]. The binding energies of Fe (2p_{3/2}) components for 10-FeZr sample were located at 708.4, 710.9, 713.0 and 719.0 eV. The binding energies were shifted slightly which implies that the Fe phase in ZrO₂ might be different from bulk iron oxide species. With little variation, the peak positions are consistent with values reported in the literature [38,39]. Accordingly, the peak at 713.0 eV in figure can be assigned to Fe phase of Fe incorporated into ZrO₂ crystallites. Droubay and Chambers reported that this kind of peak is mostly caused due to the Fe³⁺ cations at the surface of α-Fe₂O₃, which affects the binding energy of the sample [39]. The peaks at 708.4 and 710.9 eV can be assigned to disperse Fe₂O₃ type clusters.

The 2p_{3/2} peaks appeared at 706.3, 710.9, 711.5 and 719.0 eV for 20-FeZr sample. It is interesting to note that the intensity of the peaks which was assigned to Fe phase of Fe incorporated into ZrO₂ was increased significantly and intensities of the peaks due to disperse Fe₂O₃ clusters were decreased. These observations indicate that increased iron oxide loading led to an increase of metal-support interactive species. From these XPS results, it can be concluded that at least three kinds of distinctly different Fe³⁺ species are existed on the ZrO₂ surface. It is also possible to say that two kinds of dispersed Fe³⁺ species and Fe₂O₃ particles are formed on the surface of ZrO₂. The Fe³⁺ oxide clusters interacting strongly with the ZrO₂ surface.

The deconvoluted spectra of Ni (2p_{3/2}) components for 10-NiZr and 20-NiZr samples are shown in Fig. 6(D). The main peak at 855.6 eV is a representative of Ni in +2 oxidation state. Two peaks at 861.4 and 866.0 eV are shake up peaks [36]. The spectral results indicating that nickel occurs on the ZrO₂ surface mainly as NiO. In these samples, the binding energy for Ni (855.6 eV) was very close value of Ni in NiO (855.2 eV). Very close binding energy value of Ni²⁺ and same intensity of the peak in both 10-NiZr and 20-NiZr samples, revealing that nickel oxide loading on ZrO₂ did not affect the environment of Ni, probably due to the weak interaction between NiO and ZrO₂. The spectral results indicated that nickel existed on the ZrO₂ surface mainly as NiO.

The degrees of dispersion of iron, nickel and zirconium atoms on the surface of the catalysts, estimated by XPS, are shown in Table 3. From these values, as expected, the surface of 10-FeZr and 20-FeZr catalysts was enriched with iron atoms and zirconium atoms decreased as the iron oxide loading increased from 10 wt% to 20 wt%. Simultaneously, the quantity of iron on the surface fell. This effect may be due to the strong interaction between iron oxide and ZrO₂, which probably favors the transport of iron atoms into the bulk structure of ZrO₂. In contrast, there is a large amount of nickel

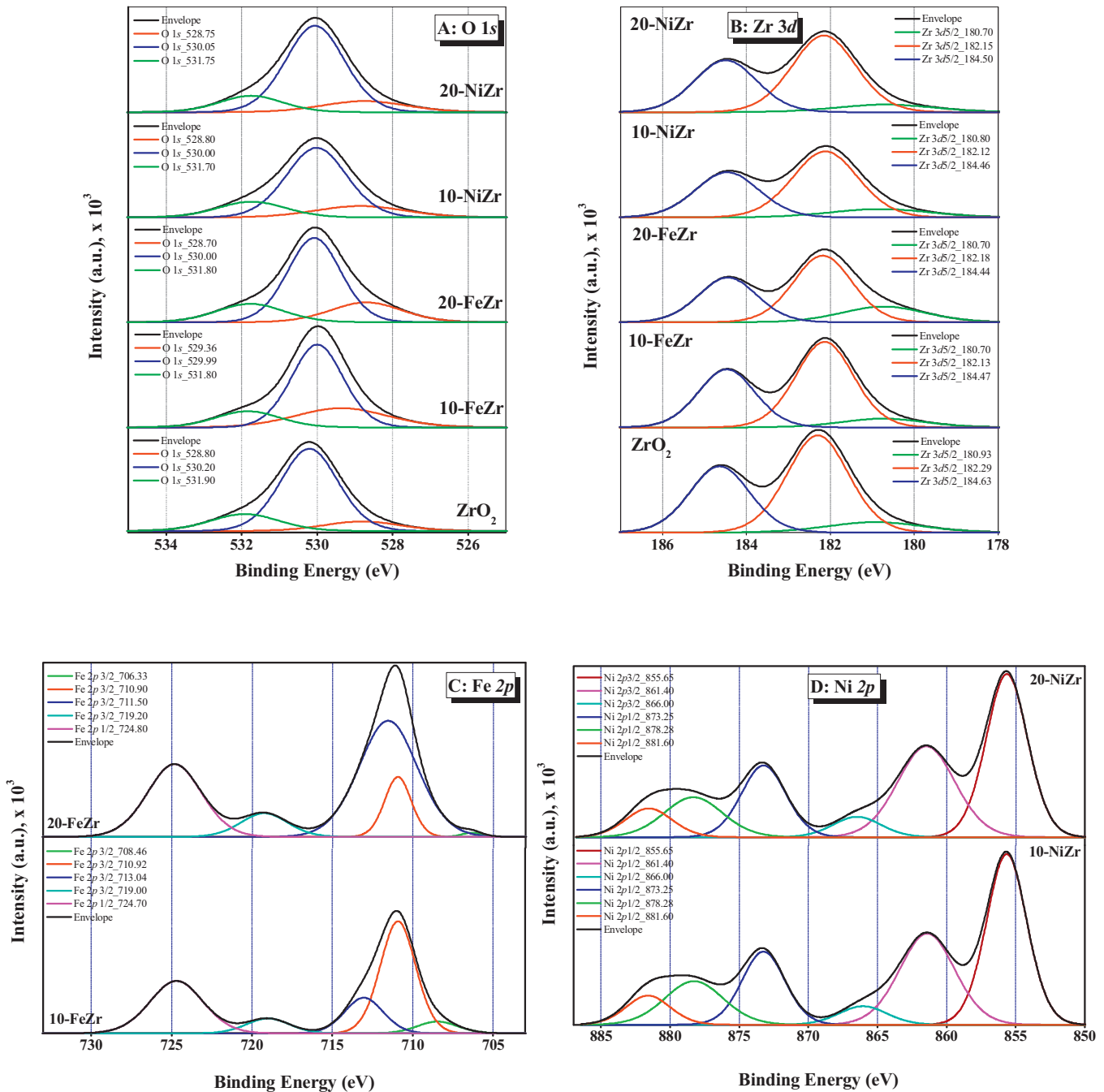


Fig. 6. (A) Deconvoluted O 1s spectra of all the catalysts. (B) Deconvoluted Zr 3d spectra of all the catalysts. (C) Deconvoluted Fe 2p spectra of 10-FeZr and 20-FeZr catalysts. (D) Deconvoluted Ni 2p spectra of 10-NiZr and 20-NiZr catalysts.

on the surface of 10-NiZr and 20-NiZr samples, compared to that on the surface of the iron oxide supported samples, owing to the weak interaction between NiO and ZrO₂ (as found in XRD and TPR analyses) that did not favor the internal diffusion of NiO into the bulk of ZrO₂.

3.8. Acidity and reducibility of the catalysts

Pyridine is a frequently used basic probe molecule to characterize the surface acidity of solid catalysts. DRIFT spectroscopy of adsorbed pyridine was used to determine the influence of the iron and nickel oxide deposition on the nature of the acid sites of the supported ZrO₂ catalysts. Fig. 7 (A) shows the FTIR spectra of pyridine (Py) adsorption at 100 °C followed by evacuation

at the same temperature on the ZrO₂, 10-FeZr, 20-FeZr, 10-NiZr and 20-NiZr samples. It is known that pyridine adsorbed samples exhibit peaks at 1446, 1486 and 1536 cm⁻¹. The peak 1446 cm⁻¹ is characteristic of Lewis-coordinated pyridine (L), whereas the band at 1536 cm⁻¹ was due to Bronsted-coordinated pyridine (B), and the band at 1486 cm⁻¹ is due to Lewis- and Bronsted-coordinated pyridine (L+B) [40].

The pure ZrO₂ sample showed a small peak at 1486 cm⁻¹ which is due to minor contribution of Lewis and Bronsted acid sites. However, a major difference was noticed in FTIR spectra of 10-FeZr and 20-FeZr samples. The formation of new Lewis sites was clearly observed as revealed by the intense bands at 1446 cm⁻¹ along side of intense peak due to Lewis and Bronsted acid sites. The Lewis acid sites density for all the catalysts was determined. Pure ZrO₂

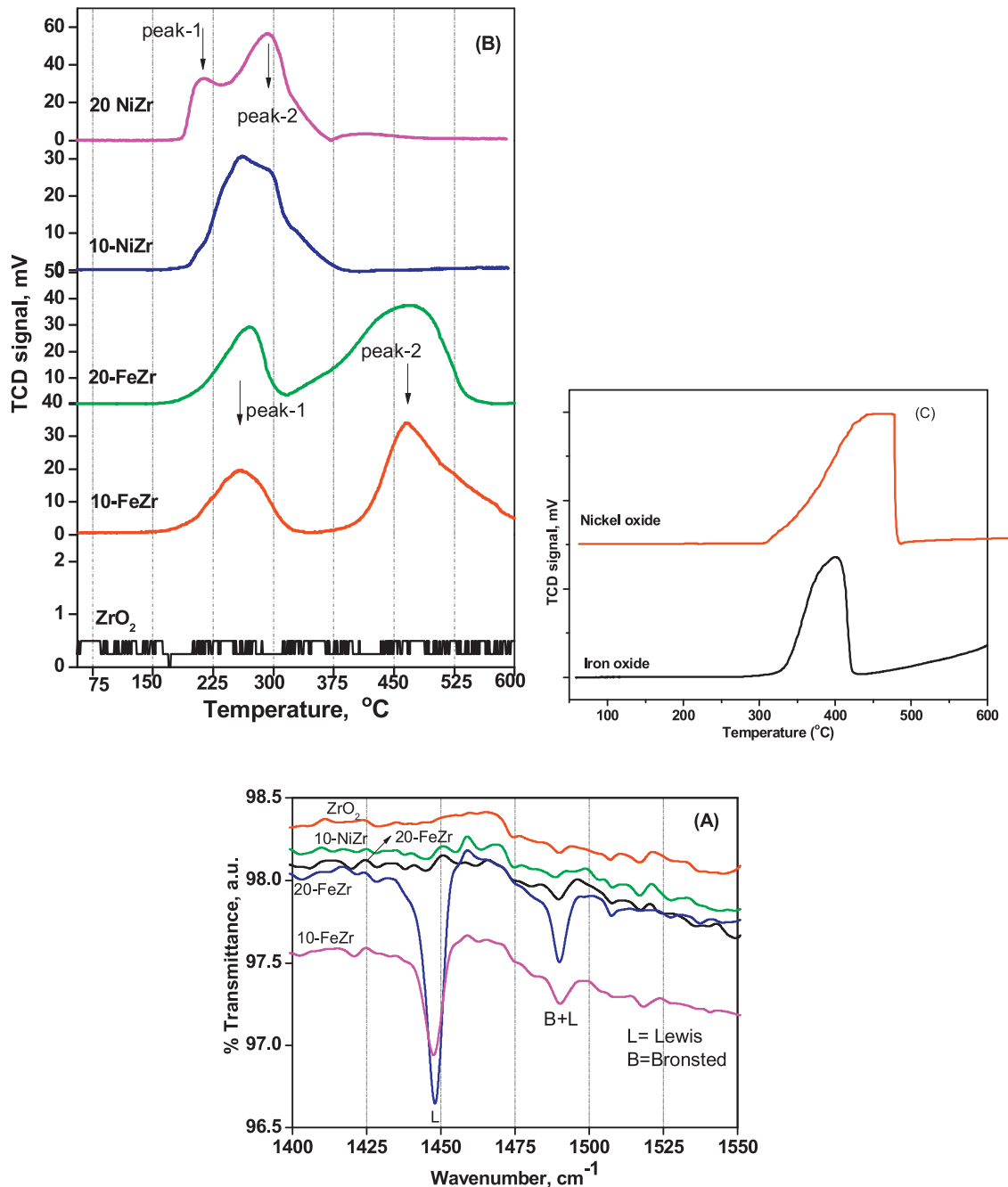


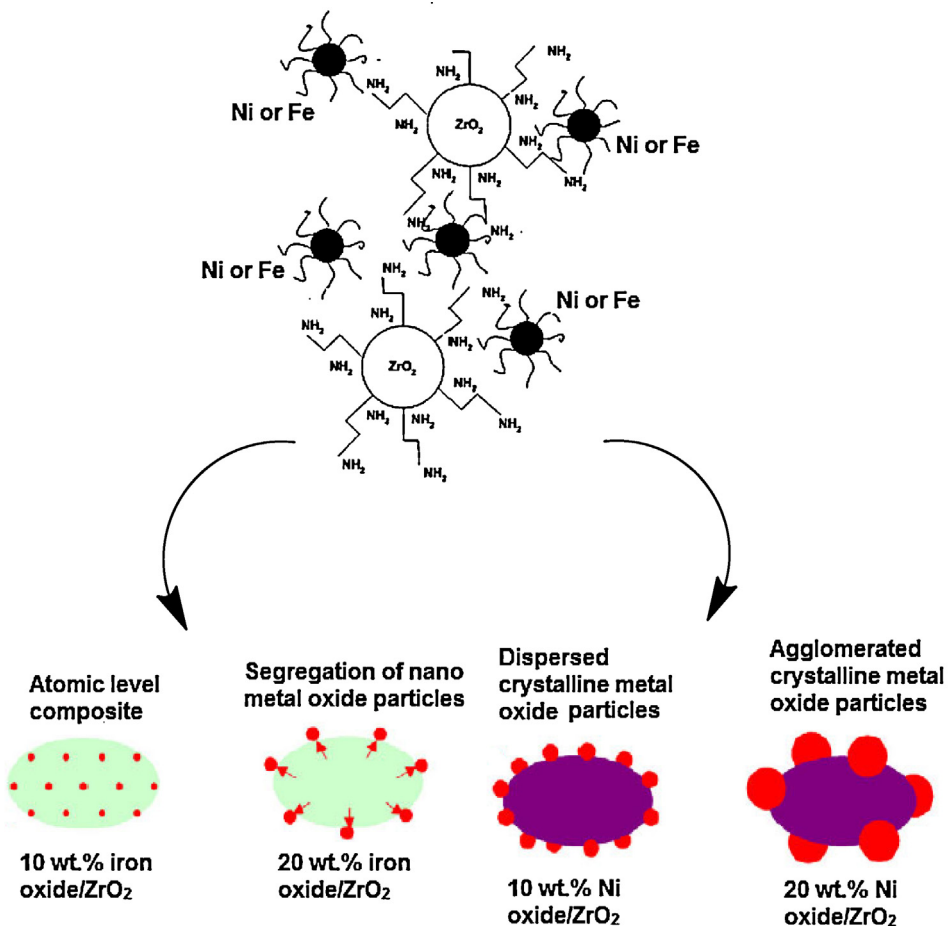
Fig. 7. (A) FTIR pyridine desorption spectra. (B) H_2 -TPR patterns of the ZrO_2 and supported catalysts. (C) H_2 -TPR of bulk iron and nickel oxides.

possessed a Lewis acid sites density of 0.9; however, after deposition of iron and nickel oxides resulted increase of density of Lewis acid sites. FeZr (20-FeZr = 42.3, 10-FeZr = 30.1) samples showed superior Lewis acid site density than NiZr (20-NiZr = 3.5, 10-NiZr = 3.0) samples. The surface species responsible for acidity in these samples are coordinated unsaturated metal ions (Fe^{3+} and Zr^{4+} ions). These cations possess an uncompensated positive charge and coordinate molecules with a free electron pair and act as Lewis acid sites [41]. Conversely, the amount of Lewis acid sites at 1446 cm^{-1} decreased after deposition of nickel oxide on ZrO_2 support. Such decrease is presumably due to the agglomeration of nickel oxide on the surface of ZrO_2 support.

The reducibility of the catalysts was determined by H_2 -TPR. H_2 -TPR patterns of the samples are shown in Fig. 7 (B). Pure ZrO_2 support did not show any reduction peaks under the studied

temperature range ($25\text{--}600\text{ }^{\circ}\text{C}$), this is because ZrO_2 is generally reduced at very high temperature. There appeared two distinct reduction peaks at low and high temperatures (peak 1 and peak 2) for 10-FeZr and 20-FeZr samples. This observation clearly indicates that there are at least two different types of iron oxide species on the surface of ZrO_2 .

It is well known that low temperature and high temperature TPR peaks of metal oxide-supported catalysts are corresponding to weak and strongly interactive species [42]. High and low temperature reduction peaks (1 and 2) in Fig. 7 (B) represent iron oxide species that were strongly and weakly interacted with ZrO_2 , respectively. It is important to note that the area of peak 2 for both iron oxide supported sample was much larger than that of peak 1, implicating that more iron oxide species are strongly interacted with ZrO_2 and only relatively small fraction of iron oxide was



Scheme 2. Schematic representation of existence of iron oxide and nickel oxide nanoparticles on the ZrO_2 support.

weakly interacted with ZrO_2 . The nickel oxide supported ZrO_2 samples also exhibited two different TPR peaks (peak 1 and peak 2). However, the reduction temperatures of nickel oxide supported samples were completely different. The reduction temperature of 10-NiZr (215°C) and 20-NiZr (235°C) were lower than that of the 10-FeZr and 20-FeZr samples (ca. 250°C). As for the temperature of peak 2, the value for 20-NiZr was lowest (only 293°C), and this peak for 10-NiZr was centered at 300°C . In contrast, the peak 2 of 10-FeZr and 20-FeZr appeared at much high temperature (460°C). H_2 -TPR patterns of bulk iron and nickel oxides are presented in Fig. 7(C) for comparison. It can be observed that bulk iron oxide showed a primary reduction peak at 380°C . H_2 -TPR of bulk nickel oxide, prepared from $\text{Ni}(\text{NO}_3)_2$ by calcination, showed a single broad reduction peak between 300°C and 400°C . In comparison to reduction temperatures of bulk oxides, the high temperature reduction peak shifted to higher temperatures in case iron oxide supported ZrO_2 samples, in contrast the reduction temperatures of high temperature peak was lowered in case of nickel oxide supported samples. It is known that the reduction of metal oxide inside the mesopores is more difficult because of the strong interaction between the metallic ion and the support [43]. The nickel oxide species had little or no interaction with ZrO_2 support, since it did not form significant chemical bonds with ZrO_2 . When Ni loading increased from 10 wt% to 20 wt%, the intensity of lower-temperature peak increased, and the peak shifted to lower temperature, indicating that more isolated nickel oxide species was present on the surface of the support, which was in agreement with the finding in XRD patterns that intense diffraction peaks from bulk nickel oxide species at $2\theta = 37.2^\circ$ and 43.3° were observed in the XRD pattern of 20-NiZr sample. The above results clearly

indicate that the interaction between iron oxide ZrO_2 is different than that of interaction between nickel oxide and ZrO_2 . The interaction between iron oxide and ZrO_2 is strong and it appears that the higher the loading and the more the number of highly interactive species.

3.9. Discussion

From the characterization data, it appears that the nickel oxide particles were set on a bulk of ZrO_2 particles with fixed-frame structure. Under heat treatment, metal oxide particles sinter and agglomerate readily and this effect was more pronounced when the nickel oxide loading was increased to 20 wt%. Since the solubility of iron oxide is more than the nickel oxide in the ZrO_2 lattice [44], atomic level composite was formed in the case of iron oxide doped ZrO_2 materials. Accordingly, the metal-support interaction in the catalyst could be strengthened with increased interfacial area, expectedly leading to improved catalytic performance. Ideally, the frame structure of the catalyst is composed of comparable nanosized nickel oxide and ZrO_2 particles (Scheme 2); the loading of nickel oxide and iron oxide particles are helping the construction of the pore structure instead of blocking it resulting in an increased surface area.

In our previous investigation, we examined the crystallization products of the ZrO_2 - Fe_2O_3 system obtained by the co-precipitation method. XRD, Raman, FTIR, TEM and XPS characterization data indicated that Fe stabilized the tetragonal ZrO_2 relatively at low temperature. However, the type of stabilized polymorph (tetragonal or cubic ZrO_2) depended on the preparation conditions used [44]. Davison et al. [45] reported the formation

of solid solutions between $\alpha\text{-Fe}_2\text{O}_3$ and ZrO_2 by the decomposition of metal nitrates. After calcination in air at 600 °C, they found cubic solid solution for 10, 15 and 20 wt% Fe^{3+} . Berry et al. [46] showed that the incorporation of Fe^{3+} ions within tetragonal ZrO_2 lattice at 500 °C stabilizes the cubic form and inhibits its transformation into the monoclinic form. The observations of the present work are in accordance with the literature reports.

The literature is not clear on the function of NiO as a stabilizer for ZrO_2 . Ni^{2+} ions are similar in size to Zr^{4+} [47] but the solubility of Ni^{2+} in ZrO_2 is not well-known. Despite relatively wide-spread commercial use of NiO-ZrO_2 systems, there exist few studies which have examined the interaction between NiO and ZrO_2 with the aim to determine the tetragonal or cubic ZrO_2 phase stability [15,48]. There is still some controversy concerning the effect of NiO on ZrO_2 phase stabilization. Dongare et al. also found that the presence of NiO stabilizes the cubic phase of ZrO_2 [15].

Friedel-Crafts alkylation is an aromatic electrophilic substitution reaction in which the carbocation is formed by the complexation of alkyl halide with catalyst [49]. The carbocation attacks the aromatic species for alkylation and hence formation of carbocation is an important step in the reaction mechanism. Lewis acidic centers on the catalyst surface facilitate the carbocation formation [50]. Thus strong Lewis acid sites may be considered to be involved in the benzylation of benzene with benzyl chloride. The 20- FeZr catalyst surface provides mostly strong Lewis acid sites; the above observations clearly indicate the dominating impact of strong Lewis acid sites for the benzylation of benzene with benzyl chloride. As observed in the FTIR pyridine adsorption results, 20- FeZr possessed high number of strong Lewis acid sites and showed highest benzylation activity.

The different spacing and symmetry of the $\text{Zr}-\text{O}$ and $-\text{OH}$ bonds on the surface of ZrO_2 particles are considered to play key roles in determining the dispersion of the active metal component and hence the catalytic properties of the metal oxide supported ZrO_2 materials [51]. It is also reported that in case of iron oxide supported benzylation catalysts generally the catalytic benzylation activity depends on the iron oxide content present. The catalyst with the highest iron oxide content showed the highest catalytic activity [52]. Hamdy et al. [53] demonstrated that the nanoparticles of iron oxide were less coordinately saturated because of lattice strain and defects than isolated iron species or the iron centers present in larger particles, thereby giving rise to more active sites. Leng et al. reported that the presence of more iron oxide nanoclusters could contribute to the improvement of catalytic activity [7]. These findings clearly corroborate with the observed results.

4. Comparison of iron oxide supported ZrO_2 catalysts with other reported catalysts

Comparison of iron oxide ZrO_2 supported catalysts with other reported catalysts was tabulated and is presented in supplementary information. In comparison with previous reports on mesoporous iron supported catalysts in the benzylation of benzene with benzyl chloride, 20- FeZr catalyst is equally efficient catalyst as other reported iron containing mesoporous catalysts. It was reported that Fe-MCM-41 [54] exhibited 90% conversion of benzyl chloride with 95% selectivity towards diphenylmethane; however, this catalyst has a major disadvantage that almost 33% of the iron atoms have been removed from the framework of MCM-41. Sun et al. [55] reported that 10 wt% iron oxide loaded SBA-15 catalyst showed 100% conversion of benzyl chloride after a reaction time of 30 min and 15 wt% iron oxide loaded SBA-15 gave 100% conversion after a reaction time of 45 min. Leng et al. [7] synthesized iron-containing mesoporous mordenite zeolite catalyst by ion-exchanged method and applied catalyst for benzylation of benzene by benzyl chloride.

The authors observed 100% conversion in just 30 min of reaction time. However, there are serious questions about the heterogeneous nature and reusability of iron exchanged porous zeolite and SBA-15 catalysts.

Shinde and Sawant [11] used various ferrites such as CuFe_2O_4 , NiFe_2O_4 , CoFe_2O_4 , ZnFe_2O_4 , and MgFe_2O_4 for benzylation of benzene with benzyl chloride. Among the catalysts, ZnFe_2O_4 offered 100% conversion of benzyl chloride in 10 min at 70 °C. CoFe_2O_4 and NiFe_2O_4 took longer reaction times, 80 min and 60 min, respectively, for 100% conversion of benzyl chloride. In the case of CuFe_2O_4 and MgFe_2O_4 there was no conversion observed. The authors did not present data on the selectivity of diphenylmethane, moreover the ferrite samples are micropores in nature with low surface area and there is a clear possibility for the diffusional problems. Koyande et al. [10] observed maximum 80% of diphenylmethane yield over sulfate-promoted $\text{ZrO}_2-\text{Fe}_2\text{O}_3$. It was observed that the activity of the catalyst decreased drastically in the second run itself and suffered gradual loss in activity.

Although in the above works the amounts of catalyst and benzyl chloride are different from those used in this work, it can be estimated that 20- FeZr is still a very active catalyst in this reaction after the effect factor of amounts of catalyst and benzyl chloride is deducted. The main advantage of using nanosized iron oxide supported on mesoporous ZrO_2 catalyst in this reaction is its higher thermal, hydrothermal and water stability as compared to other mesoporous catalysts [56]. And also as previously reported, iron species enters into crystalline structure of ZrO_2 to stabilize its tetragonal or cubic phase and it is very difficult to remove the incorporated iron species from the crystalline framework of ZrO_2 .

5. Reusability of the iron oxide supported ZrO_2 catalysts

The reusability is one of the main advantages of heterogeneous catalysts. To test reusability of iron oxide supported ZrO_2 catalysts, benzylation of benzene with benzyl chloride reaction was carried out using 20- FeZr catalyst at 80 °C. The conversion levels of benzyl chloride of this catalyst for six consecutive cycles were determined. The fresh catalyst offered 90% conversion at a reaction time of 600 min correspondingly the first and second reused catalysts presented an exactly same activity. A slight decrease of conversion (88%) was observed in fourth, fifth and sixth cycles; this could be due to loss of catalyst amount during the reaction recycling. These results indicate that the catalyst could be reused and maintain considerably good activity even after six cycles. Such catalytic performance is of great importance for potential industrial application.

6. Conclusions

Nanosized mesoporous iron and nickel oxide supported ZrO_2 catalysts were successfully synthesized using ethylenediamine as precipitating agent under isothermal conditions. Iron oxide supported ZrO_2 catalysts offered high catalytic activity than nickel oxide supported ZrO_2 catalysts in benzylation of benzene reaction under identical reaction conditions. Pure ZrO_2 consists of mixture of tetragonal and monoclinic phases, but the phase of ZrO_2 was transformed into cubic after impregnation of iron and nickel oxides. The XPS results of the iron oxide supported ZrO_2 catalysts evidently indicate that highly dispersed Fe^{3+} species are preferentially formed on ZrO_2 support and the dispersion of the Fe^{3+} species depends on the iron oxide loading that were in agreement with the XRD observations. TPR results suggested that these Fe^{3+} species strongly interacted with ZrO_2 , resulting the formation of stable $\text{Fe}^{3+}-\text{O}-\text{Zr}^{4+}$ bonds; in contrast, the nickel oxide was agglomerated into bulk particles due to its weak interaction with ZrO_2 support.

The superior catalytic activity of 20-FeZr (20 wt% iron oxide) catalyst could be due to its high iron content and porous structure, which provided larger active sites with accessible Lewis acidity.

Acknowledgments

This project was supported by the NSTIP strategic technologies program in the Kingdom of Saudi Arabia – Project no. (8-NAN184-3). The authors also, acknowledge with thanks Science and Technology Unit, King Abdulaziz University for technical support. The authors are grateful to Prof. Suprakas Sinha Ray from nano-structured materials, South Africa for his help in Raman analysis.

Appendix A. Supplementary data

Supplementary data associated with this article can be found, in the online version, at <http://dx.doi.org/10.1016/j.apcata.2014.08.012>.

References

- [1] G.A. Olah, Friedel-Crafts Chemistry, Wiley, New York, 1973.
- [2] T.W. Bastock, J.H. Clark, Specialty Chemicals, Elsevier, London, 1991.
- [3] J.H. Clark, A.P. Kybett, D.J. Macquarrie, S.J. Barlow, P. Landon, *J. Chem. Soc. Chem. Commun.* 18 (1989) 1353–1354.
- [4] B. Coq, V. Gourves, F. Figueiras, *Appl. Catal. A* 100 (1993) 69–75.
- [5] V.R. Choudhary, S.K. Jana, *Appl. Catal. A: Gen.* 224 (2002) 51–62; V.R. Choudhary, S.K. Jana, N.S. Patil, S.K. Bhargava, *Micro. Meso. Mater.* 57 (2003) 21–35.
- [6] A. Vinu, D.P. Sawant, K. Ariga, K.Z. Hossain, S.B. Halligudi, M. Hartmann, M. Nomura, *Chem. Mater.* 17 (2005) 5339–5345;
- [7] Z. Lei, S. Bai, L. Dang, H. Xia, Q. Xu, Y. Cao, L. An, M. Zhao, A.-Y. Lo, S.-B. Liu, *Micro. Meso. Mater.* 123 (2009) 306–313.
- [8] K. Leng, S. Sun, B. Wang, L. Sun, W. Xu, Y. Sun, *Catal. Commun.* 28 (2012) 64–68.
- [9] Y. Okamoto, T. Kubota, Y. Ohto, S. Nasu, *J. Catal.* 192 (2000) 412–422.
- [10] M. Sivakumar, A. Gedanken, Z.Y. Zhong, L.W. Chen, *New J. Chem.* 30 (2006) 102–107.
- [11] S.N. Koyande, R.G. Jaiswal, R.V. Jayaram, *Ind. Eng. Chem. Res.* 37 (1998) 908–913.
- [12] M.M. Shinde, M.R. Sawant, *J. Chin. Chem. Soc.* 50 (2003) 1221–1226.
- [13] N. Mizuno, H. Fujii, H. Igarashi, M. Misano, *J. Am. Chem. Soc.* 114 (1992), 7151–7151.
- [14] T.K. Cheung, B.C. Gates, *Top. Catal.* 6 (1998) 41–47.
- [15] T. Yamaguchi, *Appl. Catal.* 61 (1990) 1–25.
- [16] M.K. Dongare, K. Malshe, C.S. Gopinath, *J. Catal.* 222 (2004) 80–86.
- [17] S.N. Basahel, T. Tarek, K. Ali, A.A. Narasimharao, M. Bagabas, Mokhtar, *Mater. Res. Bull.* 47 (2012) 3463–3472.
- [18] L.K. Doraiswamy, M.M. Sharma, Examples and Reactor Design, 2, John Wiley, New York, 1984.
- [19] R. Srinivasan, R.J. De Angelis, G. Ice, B.H. Davis, *J. Mater. Res.* 6 (1991) 1287–1292.
- [20] T. Yamamoto, T. Tanaka, S. Takenaka, S. Yoshida, T. Onari, Y. Takahashi, T. Kosaka, S. Hasegawa, M. Kudo, *J. Phys. Chem. B* 103 (1999) 2385–2393.
- [21] P.D.L. Mercera, J.G. van Ommen, E.B.M. Doesburg, A.J. Burggraaf, J.R.H. Ross, *Appl. Catal.* 57 (1990) 127–148.
- [22] D. Gazzoli, G. Mattei, M. Valigi, *J. Raman Spectrosc.* 38 (2007) 824–831.
- [23] M. Yashima, K. Ohtake, M. Kakihana, H. Arashis, M. Yoshimura, *J. Phys. Chem. Solids* 57 (1996) 17–24.
- [24] D. Tan, G. Lin, Y. Liu, Y. Teng, Y. Zhuang, B. Zhu, Q. Zhao, J. Qiu, *J. Nanopart. Res.* 13 (2011) 1183–1190.
- [25] M. Rezaei, S.M. Alavi, S. Sahebdelfar, L. Xinmei, Zi-F. Yan, *J. Mater. Sci.* 42 (2007) 7086–7092.
- [26] J. Haber, J.H. Block, B. Delmon, *Pure Appl. Chem.* 67 (1995) 1257–1306.
- [27] F. Wyrwalski, J.-F. Lamontier, M.J. Perez-Zurita, S. Siffert, A. Aboukais, *Catal. Lett.* 108 (2006) 87–95.
- [28] L. Chen, J. Hu, R.M. Richards, *Chem. Phys. Chem.* 9 (2008) 1069–1078.
- [29] J.R. Sohn, Y.T. Kim, D.C. Shin, *Bull. Korean Chem. Soc.* 26 (2005) 1749–1756.
- [30] V.G. Deshpande, Y.G. Adewuyi, *Micro. Meso. Mater.* 148 (2012) 88–100; V.G. Deshpande, Y.G. Adewuyi, *Appl. Catal. A: Gen.* 462–463 (2013) 196–206.
- [31] J.A. Navio, M.C. Hidalgo, G. Colon, S.G. Botta, M.I. Litter, *Langmuir* 17 (2001) 202–210.
- [32] D. Wagner, D.A. Zatko, R.H. Raymond, *Anal. Chem.* 52 (1980), 1445–1445.
- [33] S. Damynova, B. Pawelec, K. Arishtirova, M.V. Martinez-Huerta, J.L.G. Fierro, *Appl. Catal. A: Gen.* 337 (2008) 86–96.
- [34] G.-T. Wei, C.-H. Wei, F.-M. He, C.-F. Wu, J. *Environ. Monit.* 11 (2009) 678–683.
- [35] K. Wandelt, *Surf. Sci. Rep.* 2 (1982) 1–121.
- [36] C.R. Brundle, *Surf. Sci.* 66 (1977) 581–595.
- [37] J.S. Corneille, J. He, D.W. Goodman, *Surf. Sci.* 338 (1995) 211–224.
- [38] Y. Gao, Y.J. Kim, S.A. Chambers, G. Bai, *J. Vac. Sci. Technol. A* 15 (1997) 332–339.
- [39] T. Droubay, S.A. Chambers, *Phys. Rev. B* 64 (2001), 205414–205414.
- [40] I. Rossetti, C. Biffi, C.L. Bianchi, V. Niciebla, M. Signoretto, F. Menegazzo, E. Finocchio, G. Ramis, A. Di Michele, *Appl. Catal. B: Environ.* 117–118 (2012) 384–396.
- [41] S.M. Kumbar, G.V. Shanbhag, F. Lefebvre, S.B. Halligudi, *J. Mol. Catal. A: Chem.* 256 (2006) 324–334.
- [42] B.H. Davis, R.A. Keogh, S. Alerasool, D.J. Zalewski, D.E. Day, P.K. Doolin, *J. Catal.* 183 (1999) 45–52.
- [43] K. Chen, Y. Fan, Z. Hu, Q. Yan, *Catal. Letts.* 36 (1996) 139–144.
- [44] G. Štefanic, B. Gržeta, S. Music, *Mater. Chem. Phys.* 65 (2000) 216–221.
- [45] S. Davison, R. Kershaw, K. Dwight, A. Wold, *J. Solid State Chem.* 73 (1988) 47–51.
- [46] F.J. Berry, M.H. Loreto, M.R. Smith, *J. Solid State Chem.* 83 (1989) 91–99.
- [47] R.D. Shannon, *Acta Crystallogr. A* 32 (1976) 751–767.
- [48] W.S. Chang, S. Chen, P. Shen, *Mater. Sci. Eng. A* 145 (1991) 113–118; G. Dhalenne, B. Bonvalot, A. Revcolevschi, *J. Am. Ceram. Soc.* 73 (1990) 1524–1528; A.C. Bose, R. Ramamoorthy, S. Ramasamy, *Mater. Lett.* 44 (2000) 203–207.
- [49] B. Coq, V. Gourves, F. Figueiras, *Appl. Catal. A: Gen.* 100 (1993) 69–75.
- [50] S.P. Ghorpade, V.S. Dharsane, S.G. Dixit, *Appl. Catal. A: Gen.* 166 (1998) 135–142.
- [51] Z.Y. Ma, C. Yang, W. Wei, W.H. Li, Y.H. Sun, *J. Mol. Catal. A* 231 (2005) 75–81.
- [52] C. Anand, S.V. Priya, G. Lawrence, D.S. Dhawale, S. Varghese, M.A. Wahab, K.S. Prasad, A. Vinu, *Catal. Today* 204 (2013) 125–131.
- [53] M.S. Hamdy, G. Mul, J.C. Jansen, A. Ebaid, Z. Shan, A.R. Overweg, Th. Maschmeyer, *Catal. Today* 100 (2005) 255–260.
- [54] A. Arafat, Y. Alhamed, *J. Porous. Mater.* 16 (2009) 565–572.
- [55] Y. Sun, S.J. Walspurger, P. Tessonniere, B. Louis, J. Sommer, *Appl. Catal. A: Gen.* 300 (2006) 1–7.
- [56] J.M. Dominguez, J.L. Hernandez, G. Sandoval, *Appl. Catal. A: Gen.* 197 (2000) 119–130.